Solid-state NMR calculations for metal oxides and gallates: Shielding and quadrupolar parameters for perovskites and related phases

Derek S. Middlemiss [a], Frédéric Blanc [a], Chris J. Pickard [b], Clare P. Grey [a,*]

[a] Department of Chemistry, State University of New York at Stony Brook, Stony Brook, NY 11794-3400, USA
[b] Department of Physics and Astronomy, University College London, Gower Street, London WC1E 6BT, UK

ABSTRACT

The NMR parameters obtained from solid-state DFT calculations within the GIPAW approach for ^{17}O- and $^{69/71}Ga$-sites in a range of predominantly oxide-based (group II monoxides, $SrTiO_3$, $BaZrO_3$, $BaSnO_3$, $BaTiO_3$, $LaAlO_3$, $LaGaO_3$, $SrZrO_3$, $MgSiO_3$ and $Ba_2In_2O_5$), and gallate (α- and β-Ga_2O_3, $LiGaO_2$, $NaGaO_2$, $GaPO_4$ and $LaGaO_3$) materials are compared with experimental values, with a view to the future application of a similar approach to doped phases of interest as candidate intermediate temperature solid oxide fuel cell (ITSOFC) electrolytes. Isotropic and anisotropic chemical shift parameters, quadrupolar coupling constants, and associated asymmetries are presented and analyzed. The unusual GaO_5 site occurring in $LaGaGe_2O_7$ is also fully characterised. In general, it is found that the theoretical results closely track the experimental trends, though some deviations are identified and discussed, particularly in regard to quadrupolar η_Q-values. The high quality of the computed results suggests that this approach can be extended to study more complex and disordered phases.

© 2010 Elsevier Inc. All rights reserved.

1. Introduction

Solid oxide fuel cell (SOFC) technologies continue to gather support for their potential use in the energy conversion and transport sectors [1]. The high temperature operation of SOFCs offers certain advantages, including mitigation of the need for expensive catalysts, and the potential for direct fuel reformation. However, the attendant disadvantages, including high cost, increased rates of material degradation, and prolonged start-up times, have led to efforts to identify electrolyte materials [2] possessing the requisite high ionic (typically O^{2-} or H^+) conductivities in the intermediate temperature (IT) range from approximately 400 to 700 °C. Focussing on O^{2-} conductors, aliovalent substitution has often been adopted as a means by which to increase the number of oxygen vacancies in a material, thereby promoting conductivity. Perovskite-related materials have been of particular interest in this regard, for the reason that they are very tolerant of substituents with a range of radii on both cationic sublattices [3–11]. Of particular note are the Sr- and Mg-doped $LaGaO_3$ perovskites, some of which display a higher O^{2-} conductivity than the conventional yttria-stabilised ZrO_2 electrolyte at lower operating temperature [3–7]; and materials in which the oxygen vacancies order, forming, for example, the related Brownmillerite phases such as $Ba_2In_2O_5$ and its doped variants [9–11], which, even in the pure form, con-

tain high concentrations of intrinsic O^{2-} vacancies. The intent of doping in the latter case is to attempt to bring the disordered phase associated with high conductivity down to more accessible temperatures. The location of the vacancies and the dopant–vacancy binding energetics play a crucial role in determining the conductivity of such materials, thereby dictating their potential use as SOFC electrolytes.

Alongside the more routinely-applied complement of diffraction-based techniques for the structural characterisation of such materials, solid-state magic angle spinning NMR (MAS-NMR) has provided valuable insights into local environments, vacancy trapping and transport [12–17]. NMR is of particular use in application to the disordered phases that often accompany increased conductivity in such materials. However, there exists a need to more firmly establish the correlations linking observed NMR parameters, such as isotropic chemical shift, chemical shift anisotropy and quadrupole coupling constants, to their originating local environments. First principles solid-state NMR calculations offer a means by which to investigate such dependences, permitting for the full inclusion of the effects of the wider crystalline environment. Model configurations of O^{2-} vacancies and dopant species may be imposed on supercells, the geometries optimised so as to arrive at the local structural equilibrium, and the corresponding NMR parameters efficiently obtained within a linear response approach. In the present work, the initial aim is to investigate the reliability of this method in application to a range of materials composed predominantly of pure phase oxides and gallates, with a view toward

extension to the doped phases of interest as candidate ITSOFC electrolyte materials. Our overarching aim is to determine the effect of dopants on local structure and vacancy ordering, mindful of the fact that doping may introduce new and highly distorted environments that are often present in low concentrations. As a consequence, the detection of such environments by NMR is typically non-trivial. Thus, a particular goal of the present study is to establish a reliable theoretical method for the determination of the parameters associated with such environments, so that we may subsequently predict where their NMR signatures will occur in experiments such as MQMAS spectroscopy [18–20], and derive the optimum conditions under which to detect such signals.

The NMR parameters relating to ^{17}O sites in group II monoxides and perovskite-related oxides will be examined first, followed by the analysis of computed $^{69/71}Ga$ parameters in a range of binary and ternary gallates, the quartz-structured phosphate, and a gallium germanate bearing trigonal bipyramidal GaO_5 coordination. Here, the Ga cation was selected as a representative B-site species occurring in a range of promising ITSOFC electrolytes [3–7]. Fivefold coordinated environments are of particular importance for the reason that they must be anticipated in perovskites containing oxygen vacancies. Furthermore, it is noted that applications of the GIPAW method to O sites in perovskites, and to Ga-bearing compounds in general, are very limited, so that the reference data obtained will be of broader utility beyond the purposes identified here. A particularly important issue for future work relates to the effects of motion on the NMR parameters. Many materials nominally of the perovskite type display deviation from the ideal $CaTiO_3$ (cubic perovskite) structure, adopting a series of tilts or distortions that are accompanied by a lowering of the space-group symmetry. As these materials are heated, they often undergo a series of phase transformations to more symmetric structures, such transformations generally being thought to be driven by modes involving essentially rigid motions of whole octahedral units [21]. Thus, it is often the case that a higher temperature structure determined by diffraction corresponds more to a time-average — rather than to a snapshot of the local structure. Furthermore, it is not clear that the time-averaging captured by diffraction need correspond directly to the averaging probed by NMR. Previous work by one of the present authors has explored similar issues, applying the combination of a quasiharmonic quantum statistical model for rovibrational motion with solid-state NMR calculations to obtain the shielding tensors in MgO at finite temperature [22]. The same author has also applied a similar combined lattice dynamics and molecular dynamics to the effects of thermal motion upon the computed NMR parameters of organic solids [23].

2. Computational method

First principles solid-state electronic structure calculations were performed using the CASTEP code [24], with the aim of computing the relevant NMR parameters for the compounds discussed above. Here, the magnetic shielding tensor at each site in the lattice is obtained by application of the gauge-including projector augmented wave (GIPAW) approach [25,26], while the electric field gradient, central to the prediction of quadrupolar properties, derives directly from the lattice structure and final electron density distribution [27]. The method innately offers a full treatment of the effects of lattice periodicity, bypassing potentially inaccurate finite cluster representations. While the calculations provide the shielding tensor (σ) at a given nuclear position, it is necessary to compute a reference shielding (σ_{ref}) so as to convert from absolute shieldings to the isotropic (iso) chemical shift (δ) directly relevant to experiment, via $\delta_{iso} = \sigma_{ref} + m\sigma_{iso}$ expressed in general form, where m is a gradient normally assumed equal to -1. Here, the

focus is upon ^{17}O- and $^{69/71}Ga$-sites, where the normal shift references for these nuclei comprise liquid H_2O and a 1 M aqueous solution of $Ga(NO_3)_3$, respectively. Achieving a sufficiently reliable theoretical treatment of such phases, including thermal effects, for the purpose of extracting a reference shielding is not straightforward, and so an alternate strategy similar to those used previously [28–30] is adopted, this being to plot experimental δ_{iso}-values for a range of materials against the corresponding computed σ_{iso} data. The reference shielding may then be obtained as the δ-axis intercept of the best-fit straight line. A number of choices arise in relation to this process: firstly, should the crystal structures of the subject materials be optimised, or fixed as in the corresponding experimental form? Secondly, should a gradient $m = -1$ be enforced in the fits to the δ_{iso}[expt.] – σ_{iso}[GIPAW] data, or should the slope be left free to vary?

In regard to the first point, it is intended that the present work shall, in due course, extend to include a range of model configurations of doped phases, for which geometry optimisations shall certainly be required, as a consequence of the distortions anticipated in the vicinities of substituted species and anion vacancies. The structures of the present test sets of materials are therefore also optimised to retain parity of treatment. Optimisation is further mandated by the fact that the experimental structures may be more representative of a thermal average than of the true local environment of each species of interest, as discussed above. However, for comparison, the NMR parameters obtained for a subset of the compounds using fixed experimental geometries are also presented. For further reference, the effects of structural relaxation upon computed NMR parameters have been discussed recently in the context of a study of the AlPO-14 microporous aluminophosphate by Ashbrook et al. [31]. Finally, where it is appropriate, the separations in energy of the fixed experimental and optimised cells, and the distinct polymorphic forms, are also provided.

In regard to the second point, no clear preference arises, and so an analysis of the effects upon the computed δ_{iso}-values of reference shieldings derived using both fixed and free gradients is presented. Conceivably, a suitable reference value for each species of interest might also be obtained by the application of a single GIPAW calculation to a compound whose experimental isotropic shift is very well defined. While this might offer definite advantages over the present method for compounds in which the coordination remains broadly that of the selected reference material, the intended application of the present reference data to the varied environments anticipated within the doped electrolyte phases advocates for the more inclusive approach outlined above. All of the structural optimisations employed a kinetic energy cut-off of 40 Ry for the plane wave basis set, and a linear point spacing of $0.04 Å^{-1}$ or smaller for the reciprocal space sampling mesh spanning the Brillouin zone. The PBE exchange–correlation functional [32] was adopted for all calculations, using ultrasoft pseudopotentials generated 'on-the-fly' for the same functional by the CASTEP code, save for Li and Ba atoms, where modified pseudopotentials were applied. More specifically, for Li, the pseudisation radius was reduced to 1.2 Bohrs, an extra 2s-projector was introduced, and the threshold for q_c-tuning was increased, all as compared with the default pseudopotential. Meanwhile, for Ba, the pseudisation radius for non-local components was decreased from 4.1 to 2.9 Bohrs, an additional 6s-projector was introduced, and the pseudisation radius for the two 5p-projectors was further decreased to 2.5 Bohrs, again as compared with the default. Full details of the pseudopotentials used are presented in the Supplementary Information. Convergence of absolute total energies with respect to numerical parameters was estimated at 2 meV/atom or lower in all cases. Optimisations were pursued until energy difference, maximum atomic force, maximum atomic displacement and maximum stress tensor component fell below

tolerances of 1×10^{-6} eV, 1×10^{-3} eV Å^{-1}, 1×10^{-3} Å and 5×10^{-3} GPa, respectively. The effect of decreasing the tolerances listed above by a further order of magnitude was investigated in a subset of the materials, yielding only minimal changes in geometry and computed NMR parameters. The maximum error in lattice constant (MELC) was adopted as a simple measure of the quality of agreement between the respective optimised and experimental structures. In each case, this straightforwardly amounts to the single largest deviation found between the theoretical and experimental cell lengths and angles, expressed as a fraction of the latter. The NMR parameters were obtained from single point calculations using the optimised geometries, applying a larger basis set cut-off of 60 Ry, and a more dense reciprocal space mesh with linear k-point spacing of 0.03 Å^{-1}. The isotropic shielding was obtained as $\sigma_{iso} = \frac{1}{3}(\sigma_{xx} + \sigma_{yy} + \sigma_{zz})$, where σ_{xx}, σ_{yy} and σ_{zz} are the principal components of the shielding tensor, ordered such that $|\sigma_{zz} - \sigma_{iso}| \geqslant |\sigma_{xx} - \sigma_{iso}| \geqslant |\sigma_{yy} - \sigma_{iso}|$. The chemical shift may then be derived as $\delta_{iso} = \sigma_{ref} + m\sigma_{iso}$; the anisotropy, as $\sigma_{aniso} = \delta_{aniso}/m = \sigma_{zz} - \frac{1}{2}(\sigma_{xx} + \sigma_{yy})$; and the asymmetry, as $\eta_{CS} = (\sigma_{yy} - \sigma_{xx})/(\sigma_{zz} - \sigma_{iso})$. The quadrupolar parameters for sites of interest may also be obtained via determinations of the electric field gradient at nuclear positions. The quadrupole coupling constant is obtained as $C_Q = eQV_{zz}/h$; and the asymmetry, as $\eta_Q = (V_{xx} - V_{yy})/V_{zz}$; where an ordering $|V_{zz}| \geqslant |V_{yy}| \geqslant |V_{xx}|$ of the principal components of the traceless electric field gradient tensor is assumed. Experimental values $Q = -0.02558$ and 0.106 barns have been used for the ^{17}O and ^{71}Ga electric quadrupole moments, respectively [27,33]. For reference, the C_Q-values presented for ^{71}Ga sites may be converted to those appropriate for ^{69}Ga by multiplying by a factor Q(^{69}Ga)/Q(^{71}Ga) = 1.598. The full and diagonalised shielding and electric field gradient tensors computed for each site in all of the materials studied are presented in the Supplementary Information. However, as an initial guide to the relative alignments of the principal axes of the tensors, the scalar products $S_{\sigma V} = |\boldsymbol{\sigma}_{zz} \cdot \boldsymbol{V}_{zz}|/|\boldsymbol{\sigma}_{zz}||\boldsymbol{V}_{zz}|$ of the normalised eigenvectors corresponding to the largest respective components are presented below.

3. ^{17}O calculations — group II monoxides and perovskite-derived oxides

3.1. Optimised structures and isotropic shifts

The materials selected for the calculation of the ^{17}O reference shielding comprise a range of group II monoxides and perovskite-related oxides, as listed in Table 1. CaO was specifically omitted, on the basis of the difficulties relating to the low-lying unoccupied Ca 3d-shell, as explored more fully in the recent article by Profeta et al. [54]. The maximum errors in the lattice constants (MELCs) obtained from the optimisations are presented in Table 1; comparisons of computed and experimental atomic coordinates (not detailed) are also undertaken. Despite clear differences in conditions, namely that the optimisations are formally performed at zero temperature, and the experimental structure determinations at finite temperature, the computed structures are all in good agreement with the experimental cells, save in the polarised tetragonal form (stable over a temperature range 278 < T < 393 K [45]) of the ferroelectric BaTiO$_3$ [43], where a large error manifests in the c lattice constant. A c/a ratio of 1.067 is obtained, which is substantially greater than the values 1.009; and 1.023 and 1.042 derived from diffraction [43] and previous Perdew–Wang functional calculations [55,56], respectively, but only slightly larger than the values 1.051 and 1.053 obtained using the BLYP and hybrid B3LYP functionals, [55] respectively. This overestimation of the ferroelectric distortion results in computed shieldings for the

two oxygen sublattices that are more widely separated ($\Delta\sigma = 80$ ppm) than the experimental shifts ($\Delta\delta = 41$ ppm). It has also been suggested that, beyond displacement along the elongated c-axis, the Ti ions in the tetragonal form might also display distortion in the $\langle 1\,1\,1\rangle$ directions [57]. Accordingly, a further optimisation combining the relaxed tetragonal geometry with a [1 1 1] displacement of the Ti ion has been performed, leading to a significant reduction in energy of approximately 2.3 kJ/mol below that of the higher symmetry P4mm cell. Here, a value $\Delta\sigma = 22$ ppm is obtained, which is in better agreement with the experimental separation. We note also the recent theoretical study of Zhang et al. [56], which suggests that the inclusion of antiferroelectric ordering may be necessary to arrive at a correct description of the tetragonal form of BaTiO$_3$. Meanwhile, the calculated shifts for the low temperature rhombohedral form (stable below T = 183 K [45]) differ from the experimental value by approximately 21 ppm for the free gradient reference, and 8 ppm with fixed gradient. Dynamical averaging, omitted within the present approach, might be expected to play an important role in both forms of this material. This is supported by the fact that averaging of the high and low δ_{iso}-values with a ratio 1:2 of weights, respectively, in the tetragonal form leads to significantly improved agreement between the experimental and theoretical data. Computed data for the high temperature cubic form (stable above 393 K [45]) have also been presented, though it is noted that dynamical averaging is likely to be particularly important in the paraelectric regime. Encouragingly, it is found that the relative energies of the optimised structures track the temperature order of stability of the various polymorphs. On a similar theme, we note that the nominally cubic SrTiO$_3$ compound hosts a quantum paraelectric or 'incipient ferroelectric' phase, wherein effects due to structural fluctuations are, again, likely to be significant [58].

Beyond the ferroelectric and paraelectric phases, the computed and experimental NMR data, and associated fits for all compounds are shown in Fig. 1, while the δ_{iso} and σ_{iso}-values obtained are presented in Table 1. Fits to the δ_{iso}[expt.] vs. σ_{iso}[GIPAW] data with free and fixed gradients, m, result in significant variations in σ_{ref} of magnitude ~8 ppm. As might be expected, the RMS errors are smaller in the fits with free gradient; the m-values obtained being close to, but lower in magnitude than the ideal of –1, indicating the presence of systematic error in the DFT results. Again, it is conceivable that some of this may arise due to the effects of thermal motion, and that this may be quite different for the various materials considered. A systematic treatment of such effects might be afforded by separate molecular or lattice dynamics simulations of each material, but this is an intensive task lying outside the scope of the present study. Proceeding with this in mind, it is therefore not clear that the fit with free gradient may be neglected, regardless of the fact that it may be viewed as formally less satisfactory than the fit enforcing m = –1. Importantly, and with a view to the application of both the present method and the computed σ_{ref}- and m-values in studies of related materials, it is found that the RMS errors in the fits amount to only a small fraction of the total range of chemical shifts, which spans approximately 600 ppm in width. Furthermore, the differences in the σ_{iso}-values obtained from the fully optimised and fixed experimental structures for selected compounds amount in the majority of cases to less than 5% of the former, the only exception arising within P4mm BaTiO$_3$, where differences of up to 10% of the former appear, the fixed structure σ_{iso}-values providing a substantially narrowed sublattice splitting $\Delta\sigma = 10$ ppm. While this now represents a significant underestimate of the experimental peak separation $\Delta\delta = 41$ ppm, it does support the suggestion made above that the overestimation of the ferroelectric distortion in the present pure DFT geometry optimisation significantly influences the computed shielding parameters. Moreover, that this substantial discrepancy arises even with

Table 1

The computed ^{17}O site isotropic shieldings, σ_{iso}; experimental isotropic chemical shifts, δ_{iso}; and shifts computed from fits to the δ_{iso}[expt.] – σ_{iso}[GIPAW] data (g.f. indicates fit with gradient m fixed to −1). MELC denotes the maximum error (%) in the optimised lattice constants relative to the corresponding values from the experimental structure cited alongside the space group. E_{rel} (kJ/mol) denotes the separation in energy of polymorphic forms, or experimental and optimised structures. The σ_{ref}-values, gradients (m) and root mean square errors obtained from the fits are also shown, along with the standard errors in the former two quantities. (expt) indicates that the fixed experimental structure was used in the calculation [34–53].

Material	Space group	E_{rel} (kJ/mol)	MELC (%)	σ_{iso} (ppm) [GIPAW]	δ_{iso} (ppm) [expt.]	δ_{iso} (ppm) [GIPAW]	δ_{iso}(g.f.)(ppm) [GIPAW]
Group II monoxides							
BeO	P6$_3$mc [34]	0	+0.8	+229.87	26 [35]	19.58	−14.04
BeO (expt.)	P6$_3$mc [34]	+0.40		+232.20	26 [35]	17.51[a]	−16.37[a]
MgO	Fm$\bar{3}$m [36]		+0.7	+198.04	47 [35]	47.85	17.79
SrO	Fm$\bar{3}$m [37]		+0.7	−205.21	390 [35]	405.93	421.04
BaO	Fm$\bar{3}$m [38]		+1.3	−444.25	629 [35]	618.20	660.08
Perovskite-derived oxides							
SrTiO$_3$	Pm$\bar{3}$m [39]	0	+0.9	−301.29	465 [40]	491.25	517.12
SrTiO$_3$ (expt.)	Pm$\bar{3}$m [39]	+2.14		−287.34	465 [40]	478.86[a]	503.17[a]
BaZrO$_3$	Pm$\bar{3}$m [41]		+1.0	−172.81	376 [40]	377.16	388.64
BaSnO$_3$	Pm$\bar{3}$m [42]		+1.4	+98.01	143[b]	136.67	117.82
BaTiO$_3$	P4mm [43]	+4.17	+5.6	−395.64	564 [44]	575.04	611.47
				−315.64	523 [44]	504.00	531.47
BaTiO$_3$	R3m [45]	0	+1.7	−330.66	538 [46]	517.33	546.49
BaTiO$_3$	P4mm [43] + Ti [1 1 1] distort	+1.83		−345.35	564 [44]	530.37	561.18
				−323.41	523 [44]	510.89	539.24
BaTiO$_3$ (expt.)	P4mm [43]	+12.36		−357.87	564 [44]	541.49[a]	573.70[a]
				−347.44	523 [44]	532.23[a]	563.27[a]
BaTiO$_3$	Pm$\bar{3}$m [43]	+16.98	+1.4	−379.30		560.52	595.13
LaAlO$_3$	R$\bar{3}$c [47]		+1.2	+69.51	170.2 [40]	161.98	146.32
LaGaO$_3$	Pbnm [48]		+1.8	+13.86	221(4)[c]	211.40	201.97
				+11.01	221(4)[c]	213.93	204.82
SrZrO$_3$	Pbnm [49]		−2.6	−139.54	343.7 [40]	347.62	355.37
				−135.03	340.2 [40]	343.61	350.86
MgSiO$_3$	Pbnm [50]	0	+0.8	+131.95	108(2) [51]	106.54	83.88
				+131.05	108(2) [51]	107.33	84.78
MgSiO$_3$ (expt.)	Pbnm [50]	+1.47		+138.53	108(2) [51]	100.69[a]	77.30[a]
				+137.44	108(2) [51]	101.65[a]	78.39[a]
Ba$_2$In$_2$O$_5$	Ima2 [52]/Ibm2 [53]		+2.2	+50.14	184[d]	179.19	165.70
				+33.31	184[d]	194.13	182.52
				+71.83	137[d]	159.93	144.01
σ_{ref} (ppm)						223.70 ± 3.03	215.83 ± 5.90
m						−0.888 ± 0.014	−1
RMS error (ppm)						12.1	25.7

[a] δ_{iso}-value computed for fixed experimental structure via reference values obtained from the set of fully optimised structures. Shading indicates value not included in calculation of reference shielding.

[b] Buannic et al. (unpublished data).

[c] Blanc et al. (unpublished data).

[d] The ^{17}O parameters for Ba$_2$In$_2$O$_5$, although originally reported by Adler et al. [16] have been reanalyzed recently, the latter data being presented here (Holmes et al., unpublished data).

use of the experimental geometry points to the difficulties inherent in reconciling the averaged diffraction structure with the local environments experienced by the O nuclei on the NMR timescale. Proceeding, an examination of the δ_{iso}-values derived from the fixed experimental structures via the shielding references presented above reveals no clear systematic improvement in quality of agreement with the experimental data. A more meaningful comparison might be achieved by re-deriving the reference values from a full set of NMR parameters obtained from the fixed experimental structures, but, again, this exceeds the scope and purpose of the present study.

3.2. Chemical shift anisotropies, asymmetries and quadrupole parameters

Computed quantities relating to the anisotropy of and asymmetry in the shielding tensor and quadrupole tensor are presented in Table 2. Experimental values, where available, are also shown, though it should be noted that the determination of such quanti-

ties by fitting of the spectra is often hindered by difficulties in separating features due to chemical shift anisotropy (CSA) and quadrupolar interactions [40]. Discussing the group II monoxide data first, a lack of experimental CSA determinations is evident, which, for MgO, SrO and BaO at least, is in keeping with the cubic symmetry at the O sites. Finite σ_{aniso} is permitted by symmetry in BeO, though, again, no experimental data was found. Here, use of the fixed experimental structure leads to a significant increase in σ_{aniso} amounting to approximately 8% of the value obtained from the fully optimised structure, while the η_{CS}-values do not differ noticeably. The experimental C_Q-values for MgO, SrO and BaO are all low as expected; Turner et al. [35] attribute the larger value in MgO to the presence of significant distortions, though it is suggested here that the presence of lattice defects may be the most significant contribution to the experimentally observed non-zero value of the quadrupole interaction. It should be noted, however, that the cubic symmetry of all three of the aforementioned materials means that C_Q-values of zero must be expected. The significant non-zero value for wurtzite-structured BeO is, again,
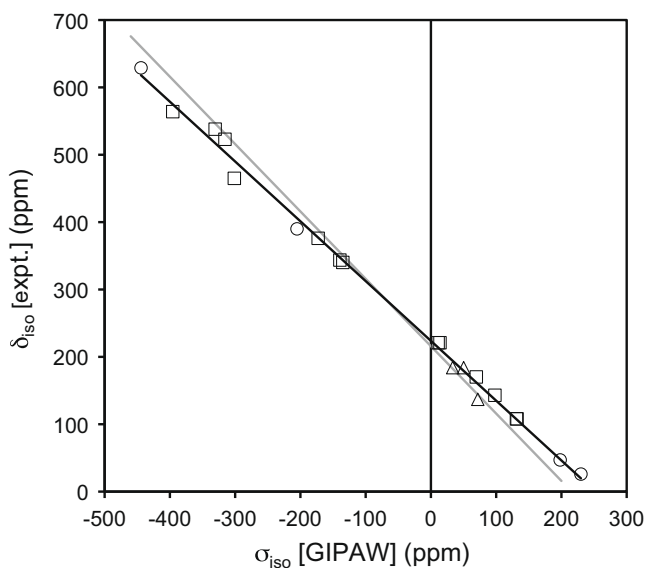
Fig. 1. Plot of experimental isotropic shift, δ_{iso} (ppm), against computed isotropic shielding, σ_{iso} (ppm), for ^{17}O sites, with associated linear fits. Circles denote group II monoxide data; squares, perovskite-derived oxide data; and triangles, defect-perovskite (Brownmillerite $Ba_2In_2O_5$) data. Black line denotes the best fit with free gradient; and the grey line, a fit with gradient fixed to –1.

permitted by symmetry, and is qualitatively reproduced by the calculations: the value obtained from the fixed experimental structure being in marginally better agreement with experiment. As expected, the η_Q-values at this site are zero, with the major axis of the EFG tensor oriented along the c-axis of the hexagonal cell, and the two minor axes confined to the ab-plane. Moreover, the $S_{\sigma V}$ values indicate collinearity of the largest principal components of the CS and EFG tensors.

Comparison of the CSA data for the perovskite-derived materials is possible in only a small number of cases. For SrTiO3 and BaZrO3, computed anisotropy values in excellent agreement with experiment are obtained, bearing in mind that opposite signs are anticipated for δ_{aniso} and σ_{aniso}. It is also found that the σ_{aniso}-value computed for SrTiO3 with the fixed experimental structure is in marginally better agreement with experiment. Proceeding directly from the symmetry of these lattices, the calculated η_{CS}-values are zero, in contrast with the finite values obtained from Herzfeld–Berger analyses of the experimental spectra [40]. These discrepancies may point to the difficulties inherent to such analyses in these materials, as a consequence of the contribution of the second-order quadrupolar interaction to the spinning sideband intensities [40], and the difficulties in separating this effect from the CSA without recourse to the analysis of spectra at multiple field strengths. Similar difficulties likely contribute to the inferior agreement of experimental and computed CSA and asymmetry parameters in LaAlO3 and LaGaO3, the effect being further compounded by the small magnitude of the CSA in these materials. In BaTiO3, the difference between the σ_{aniso}-values for the two sublattices is greater than for those obtained experimentally. Again, this is attributed to a combination of motional effects with the overestimation of the ferroelectric distortion in the present theoretical approach. Interestingly, the CSA values obtained for the latter compound with the fixed experimental structure are in markedly better agreement with experiment, a substantial reduction in η_{CS} from 0.51 to 0.12 also being obtained for the O sublattice with lower δ_{iso}-value.

In contrast, experimental quadrupole-related parameters are available for a wider range of materials, though it should be noted that, in many cases, the quoted C_Q-values represent upper esti-

mates based upon the centre band linewidths (denoted (max) in Table 2). Encouragingly, it is found that the calculated C_Q-values are always of smaller magnitude than the quoted maxima. More definitive experimental C_Q- and η_Q-values have been determined for LaAlO3, LaGaO3 and MgSiO3, and C_Q-values for $Ba_2In_2O_5$. The agreement of the computed results with these data is noticeably better, which is a significant finding given the complex octahedral tilts and O environments typical of the latter three materials. Application of the fixed experimental structures of SrTiO3 and MgSiO3 yields no improvement in C_Q-value in the former material, and only marginal improvement in the latter case, though our earlier point in relation to the possible influence of the paraelectric fluctuations in SrTiO3 should be borne in mind. In tetragonal BaTiO3, meanwhile, use of the experimental structure leads to closer C_Q- and η_Q-values for the two sublattices. Finally, examination of the $S_{\sigma V}$ values reveals that, in the majority of perovskite-related structures, the largest principal components of the CS and EFG tensors are either close to or are precisely collinear. Exceptions to this trend occur in SrZrO3, in which an either near or precisely orthogonal orientation manifests depending upon the sublattice examined; and in $Ba_2In_2O_5$, where one of the sublattices also displays a near-orthogonal arrangement.

4. $^{69/71}Ga$ calculations — oxides, phosphate and the GaO5 site in LaGaGe2O7

4.1. Optimised structures and isotropic shifts for GaO4 and GaO6 compounds

As stated above, Ga was chosen as a representative B-site cation featuring in materials with potential applications as ITSOFC electrolytes. Given that the focus in such phases is upon the effects of aliovalent doping and the O^{2-} vacancies introduced thereby, it is important to test the sensitivity of the present method to the coordination of Ga cations. Thus, a range of materials featuring typical GaO6, GaO4, and a more unusual GaO5 environment was selected. The latter coordination, manifesting in the LaGaGe2O7 compound [59], merits the separate detailed discussion presented later in this section. On the basis of MELCs and comparisons of atomic coordinates (not detailed), it is again found that the optimised structures achieve an acceptable quality of agreement with experiment.

The δ_{iso}- and σ_{iso}-values, and computed fit parameters are displayed in Fig. 2 and Table 3. Again, the choice of whether to fix the gradient in the linear fits to the δ_{iso}[expt.] vs. σ_{iso}[GIPAW] data leads to significant variations in the computed σ_{ref}-value, amounting to some 213 ppm. The RMS errors obtained from the fits parallel those discussed above for O sites, in that the RMSE achieved by the free-gradient line is approximately one-half that of the more constrained fit. Both sets of computed δ_{iso}-values track the experimental trends across the range of environments well, including the anomalous shift observed for GaPO4, which, despite its origin in a tetrahedral site, presents a value closer to that expected for sixfold coordination. Again, the fitted gradient is close to, but lower in magnitude than the formal value of –1, presumably for reasons similar to those suggested above, namely systematic error and neglect of thermal effects. Here, as above, the application of fixed experimental structures for a subset of the materials leads to relatively small variations in σ_{iso}-values, amounting to less than approximately 3% of the values obtained with fully optimised geometries. However, for Ga sites, it emerges that, even comparatively minor fractional variations in σ_{iso} may lead to much more significant absolute variations in the corresponding δ_{iso}-values, as a consequence of the disparate magnitudes of these parameters. Thus, the δ_{iso}-values computed for the fixed structures with the

Table 2
Comparison of the experimental and computed properties related to the anisotropy of –, asymmetry in – and relative orientation of the chemical shift and electric field gradient tensors at ^{17}O sites. (max) indicates upper estimate of C_Q based upon the centre band linewidth [34–43,45,47–53].

Material	Space group	Chemical shift tensor				Quadrupole interaction tensor				$S_{\sigma v}$
		δ_{aniso} (ppm)[expt.]	η_{CS} [expt.]	σ_{aniso} (ppm)[GIPAW]	η_{CS} [GIPAW]	C_Q (MHz) [expt.]	η_Q [expt.]	C_Q MHz)[GIPAW]	η_Q [GIPAW]	
Group II monoxides										
BeO	P6$_3$mc [34]			15.57	0.04	~0.020 [35]		0.032	0.00	1.000
BeO (expt.)	P6$_3$mc [34]			16.78	0.04	~0.020 [35]		0.029	000	1.000
MgO	Fm$\bar{3}$m [36]			0.00		~0.014 [35]		0.00		
SrO	Fm$\bar{3}$m [37]			0.00		<0.005 [35]		0.00		
BaO	Fm$\bar{3}$m [38]			0.00		<0.005 [35]		0.00		
Perovskite-derived oxides										
SrTiO$_3$	Pm$\bar{3}$m [39]	−441 [40]	0.22 [40]	456.88	0.00	1.4^{max} [40]		−0.99	0.00	1.000
SrTiO$_3$ (expt.)	Fm$\bar{3}$m [39]	−441 [40]	0.22 [40]	443.03	0.00	1.4^{max} [40]		−0.81	0.00	1.000
BaZrO$_3$	Pm$\bar{3}$m [41]	−294 [40]	0.44 [40]	323.72	0.00	1.4^{max} [40]		0.62	0.00	1.000
BaSnO$_3$	Pm$\bar{3}$m [42]			37.30	0.00			−6.94	0.00	1.000
BaTiO$_3$	P4mm [43]	−520 [40]		617.60	0.00			−0.70	0.00	1.000
		−480 [40]		455.24	0.28			−1.77	0.51	1.000
BaTiO$_3$	R3m [45]			506.60	0.14			−1.30	0.11	0.992
BaTiO$_3$	P4mm [43] + Ti [1 1 1] distort	−520 [40]		539.67	0.15			−1.04	0.25	0.992
		−480 [40]		497.16	0.16			−1.40	0.17	0.988
BaTiO$_3$ (expt.)	P4mm [43]	−520 [40]		511.31	0.00			−1.36	0.00	1.000
		−480 [40]		490.28	0.05			−1.63	0.12	1.000
BaTiO$_3$	Pm$\bar{3}$m [43]			519.07	0.00			−1.78	0.00	1.000
LaAlO$_3$	R$\bar{3}$c [47]	80(30)^a	0.2(1)^a	−144.15	0.12	1.6^{max} [40], 1.21(23)^a	0.15(12)^a	−1.42	0.20	0.998
LaGaO$_3$	Pbnm [48]	30(10)^a	0.0(1)^a	−90.51	0.74	3.30(20)^a	0.17(2)^a	−3.84	0.16	1.000
				−100.80	0.82			−3.79	0.19	0.980
SrZrO$_3$	Pbnm [49]			300.91	0.19	1.2^{max} [40]		−0.55	0.76	0.000
				304.19	0.22			−0.75	0.51	0.077
MgSiO$_3$	Pbnm [50]			49.62	0.43	5.1(2) [51]	0.1(1) [51]	−5.43	0.28	1.000
				52.10	0.09			−5.44	0.13	0.997
MgSiO$_3$ (expt.)	Pbnm [50]			43.86	0.46	5.1(2) [51]	0.1(1) [51]	−5.30	0.28	1.000
				46.26	0.11			−5.31	0.12	0.997
Ba$_2$In$_2$O$_5$	Ima2 [52]/Ibm2 [53]			−84.39	0.05	5.19^b		−5.74	0.05	0.999
				135.26	0.85	5.89^b		−4.70	0.88	0.003
				−61.16	0.77			−6.28	0.14	0.924

^{a} Blanc et al. (unpublished data).
^{b} The ^{17}O parameters for Ba$_2$In$_2$O$_5$, although originally reported by Adler et al. [16] have been reanalyzed recently, the latter data being presented here (Holmes et al., unpublished data).

fitted references discussed above vary markedly from those obtained with fully optimised cells, leading in all cases to poorer agreement with the experimental data. Again, it is noted that a more meaningful comparison might be achieved via reference data re-derived from a full set of NMR calculations using the fixed structures, but that, as for O sites, this lies beyond the scope and purpose of the present study.

4.2. Chemical shift anisotropies, asymmetries and quadrupole parameters for GaO$_4$ and GaO$_6$ sites

The experimental CSA data for the Ga-bearing compounds shown in Table 4 are very limited; to the best of the present authors' knowledge, the only known values relate to the tetrahedral and octahedral sites in β-Ga$_2$O$_3$. The computed σ_{aniso}- and η_{CS}-data are in good agreement with these values in terms of magnitude, and lead to δ_{aniso}-values possessing the same sign as experiment. Application of the fixed β-Ga$_2$O$_3$ experimental structure leads to very marginal improvement in σ_{aniso}-values, but yields

no clear improvement in η_{CS}-values. Use of the fixed experimental structure in LiGaO$_2$ also yields a significant increase in σ_{aniso}. No systematic trends are evident in the calculated σ_{aniso}- and η_{CS}-values in relation to their originating coordinations. Ash and Grandinetti [61] present a comprehensive set of fitted quadrupole parameters for most of the materials, the remaining values being obtained from studies by Massiot et al. [59], by O'Dell et al. [62] and by the present authors (Blanc et al., unpublished data). The trend in the calculated values tracks the experimental C_Q-values well, though there is some appreciable deviation, tending toward underestimation, in the individual magnitudes, particularly for the octahedral site in β-Ga$_2$O$_3$. The η_Q-values show more variation, where, again for β-Ga$_2$O$_3$ in particular, the calculations indicate greater asymmetry in the EFG tensor at octahedral as compared with tetrahedral sites, in contrast with the experimental findings. However, comparison of the optimised and experimental Ga environments [63] within this compound reveals very similar mean and standard deviations in Ga–O bond lengths, so that the discrepancies in C_Q- and η_Q-values cannot be attributed to differences in
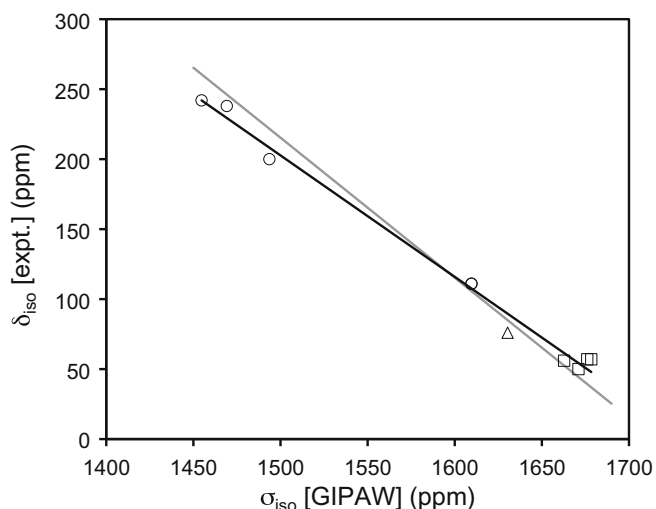
Fig. 2. Plot of experimental isotropic shift, δ_{iso} (ppm), against computed isotropic shielding, σ_{iso} (ppm), for ^{71}Ga sites, with associated linear fits. Circles denote approximately tetrahedral GaO_4 sites; squares, approximately octahedral GaO_6 sites; and triangle, the trigonal bipyramidal GaO_5 site occurring in $LaGaGe_2O_7$. Black line denotes the best fit with free gradient; and the grey line, a fit with gradient fixed to −1.

local structure, assuming that there were no issues related to the structural refinement. The fixed experimental structure calculations for α-Ga_2O_3, β-Ga_2O_3 and $LiGaO_2$ provide marginal improvements in C_Q-values for the first two of these, and a much more significant improvement for the latter. It emerges, however, that the η_Q-values for the latter two compounds are not improved by application of the fixed geometries. Again, while there is undoubtedly error in the DFT-derived NMR parameters, the contribution to these discrepancies arising out of the difficulties in fitting the experimental spectra must also be acknowledged. Finally, an examination of the $S_{\sigma V}$ values reveals that, as for O sites, the largest principal components of the CS and EFG tensors are either close to or are precisely collinear in the majority of cases. Exceptions to this trend arise for the octahedral site in β-Ga_2O_3 and in $NaGaO_2$, where orthogonal relative orientations manifest; and for the tetrahedral site in β-Ga_2O_3, where an intermediate angle arises.

4.3. GaO_5 site in LaGaGe_2O_7

The $LaGaGe_2O_7$ compound offers the best resolved and isolated spectra for the GaO_5 coordination obtained to-date [59]. Here, as mentioned above, the focus upon this particular environment arises due to the presence of fivefold coordinated sites in promising electrolyte materials such as Sr- and Mg-doped $LaGaO_3$ [3–7], in which the application of MAS NMR might readily be expected to disclose the presence of O vacancies adjoining Mg^{2+} or Ga^{3+} cations (Blanc et al., unpublished data). Tests of the ability of the present solid-state DFT approach to accurately reproduce the local structure of and NMR parameters for GaO_5 sites in this model compound therefore constitutes an important demonstration that this and similar sites in the aliovalently-doped phases can be reliably modelled. It should be noted, however, that the structural parameters quoted by Massiot et al. [59] relate not to $LaGaGe_2O_7$, but rather to the isostructural $NdGaGe_2O_7$ material [68]. Proceeding on the basis that the La^{3+} and Nd^{3+} ninefold coordinated ionic radii do not differ substantially [70], the optimised cell is found to be in reasonable agreement with experiment, a MELC of 3.66% emerging for the a-vector. Moreover, all of the cell lengths tend toward over-estimation of the $NdGaGe_2O_7$ values, in keeping with the slightly

larger La^{3+} ninefold coordinated ionic radius. Examining the Ga–O bond lengths, the optimised structure yields a mean, standard deviation, and range of 1.954, 0.073 and 0.151 Å, respectively, as compared with experimental values of 1.919, 0.074 and 0.161 Å, respectively. Similarly, for O–Ga–O bond angles, the optimised structure provides a mean, standard deviation and range of 106.96, 27.48 and 48.36°, respectively, as compared with experimental values of 107.01, 27.55 and 48.28°, respectively. The optimised coordination is such that three equatorial (eq; mean length 1.905 Å) and two apical (ap; mean length 2.028 Å) Ga–O bonds may be identified, with O_{eq}–Ga–O_{eq} angles of 133.179, 126.971 and 99.776°, and an O_{ap}–Ga–O_{ap} angle of 169.051°. The corresponding experimental distribution of bond lengths and angles is very similar. Thus, the present trigonal bipyramidal GaO_5 environment deviates significantly from the square pyramidal coordination, or distorted variant thereof, anticipated for oxygen vacancy formation in doped perovskites. Nevertheless, it is clear that the current approach faithfully reproduces the local structure of these sites in this model compound.

The experimental [59] and computed NMR parameters for GaO_5 sites in $LaGaGe_2O_7$ are compared in Tables 3 and 4 and in Fig. 2. Encouragingly, the theoretical δ_{iso}-values obtained from the reference data with free and fixed gradients lie just outwith or at the upper end, respectively, of the range established by the experimental value plus associated error. However, the computed σ_{aniso}-value exceeds by a factor of approximately two the experimentally assessed CSA of order 100 ppm obtained at high field strength, though Massiot et al. point out that their analysis of the CSA must be regarded as preliminary [59]. Examining the quadrupole-related parameters, bearing the caveats discussed above in mind, it emerges that the theoretical and experimental C_Q- and η_Q-values are in reasonable agreement: the former underestimating the latter by approximately 23% and 20% for C_Q and η_Q, respectively. Moreover, the $S_{\sigma V}$ value indicates a near-orthogonal arrangement of the largest principal components of the CS and EFG tensors.

5. Conclusions and future prospects

The results presented above demonstrate that solid-state GIPAW calculations are a reliable predictor of the NMR parameters of ^{17}O sites in mono and mixed metal oxides, and $^{69/71}$Ga-sites with varying coordination, as featured in a range of materials. The prospects for extension to a wider range of perovskite A- and B-site cations and dopants are encouraging, in that the computed chemical shift data track experimental values with acceptable accuracy. The routine use of GIPAW calculations to aid the interpretation of NMR spectra obtained from technologically-relevant doped phases may therefore be readily envisaged. This should enable more accurate NMR-based determinations of the environments disposed to host O^{2-} vacancies, while the total energies and NMR parameters obtained from supercell calculations for a range of vacancy–dopant configurations should provide further insights into the mobility of anion vacancies in these materials, and into the effects of hopping on the NMR spectra. More specifically, the key conclusions of the present study are as follows:

(i) The fitting of two forms of linear trend to the δ_{iso}[expt.] vs. σ_{iso}[GIPAW] data for O and Ga sites reveals that the choice of whether to fix the gradient at the formal value of −1, or leave it free, results in significant differences in the calculated σ_{ref}-values for both species. The fitted gradients deviate appreciably from −1, which is likely due to the combination of systematic error in the theoretical results, and the effects of dynamical averaging in the experimental determinations. It is noted, however, that in all cases the RMS errors obtained from the fits amount to only a small

Table 3
The computed ^{71}Ga site isotropic shieldings, σ_{iso}; experimental isotropic chemical shifts, δ_{iso}, and shifts computed from fits to the δ_{iso}[expt.] – σ_{iso}[GIPAW] data (*g.f.* indicates fit with gradient m fixed to −1). MELC denotes the maximum error (%) in the optimised lattice constants relative to the corresponding values from the experimental structure cited alongside the space group. E_{rel} (kJ/mol) denotes the separation in energy of polymorphic forms, or experimental and optimised structures. The σ_{ref}-values, gradients (m) and root mean square errors obtained from the fits are also shown, along with the standard errors in the former two quantities. (expt.) indicates that the fixed experimental structure was used in the calculation [48,59–68].

Material	Space group	E_{rel} (kJ/mol)	MELC (%)	σ_{iso} (ppm) [GIPAW]	δ_{iso} (ppm) [expt.]	δ_{iso} (ppm) [GIPAW]	δ_{iso} (*g.f.*) (ppm) [GIPAW]
α-Ga$_2$O$_3$ (oct.)	R$\bar{3}$c [60]	+15.26	+1.5	1662.77	56(7) [61] 52(1) [62]	61.46	52.49
α-Ga$_2$O$_3$ (expt.) (oct.)	R$\bar{3}$c [60]	+21.64		1634.54	56(7) [61] 52(1) [62]	85.93[a]	80.72[a]
β-Ga$_2$O$_3$ (oct.)	C2/m [63]	0	+1.9	1671.00	50(10) [61] 41(1) [62]	54.33	44.26
(tet.)				1493.61	200(50) [61] 201(2) [62]	208.08	221.65
β-Ga$_2$O$_3$ (expt.) (oct.)	C2/m [62]	+7.00		1640.74	50(10) [61] 41(1) [62]	80.56[a]	74.52[a]
(tet.)				1459.21	200(50) [61] 201(2) [62]	237.89[a]	256.05[a]
LiGaO$_2$ (tet.)	Pna2$_1$ [64]	0	+1.6	1454.18	242(2) [61]	242.25	261.08
LiGaO$_2$ (expt.) (tet.)	Pna2$_1$ [64]	+46		1419.88	242(2) [61]	271.98[a]	295.38[a]
NaGaO$_2$ (tet.)	Pna2$_1$ [65]		+2.8	1469.17	238(2) [61]	229.26	246.09
GaPO$_4$ (tet.)	P3$_1$21 [66]		+2.5	1609.59	111(5) [59]	107.56	105.67
LaGaO$_3$ (oct.)	Pbnm [48]		+1.8	1678.34	57(1)[b] 51.0(2) [61]	47.97	36.92
LaGaO$_3$ (oct.)	R3c [67]		+1.1	1676.04	57(1)[b]	49.96	39.22
LaGaGe$_2$O$_7$ (5-coord)	P2$_1$/c [68]			1630.35	76(10) [59]	89.56	84.91
σ_{ref} (ppm)						1502.63 ± 48.59	1715.26 ± 4.47
m						−0.867 ± 0.030	−1
RMS error (ppm)						7.27	13.41

[a] δ_{iso}-value computed for fixed experimental structure via reference values obtained from the set of fully optimised structures. Shading indicates value not included in calculation of reference shielding. (oct.) denotes octahedral site, (tet.) tetrahedral site.
[b] Blanc et al. (unpublished data).

fraction of the total range of chemical shifts of the nuclei involved, lending credibility to the present approach. This is an important point, given that the isotropic shift is, for many nuclei, often regarded as the key NMR discriminant of site coordination.

(ii) The situation as regards CSA and quadrupolar parameters is more complex, though, in general, the GIPAW-derived values track the experimental trends in a satisfactory fashion. In particular, the σ_{aniso}-parameters computed for a limited set of the perovskite-derived oxides are in good agreement with the limited experimental δ_{aniso}-data, while the η_{CS}-values differ more substantially. Comparisons for Ga sites are very limited for CSA parameters, while the computed C_Q-values again track experiment in a reasonable manner. However, some discrepancies are noted in the η_Q-values. Central to all of the foregoing points is the understanding that there are two likely sources of error in comparisons of this type. The first arises out of the limitations of the DFT calculations themselves, in particular their omission of thermal effects and their use of the space-group symmetries obtained from motionally-averaged diffraction structures. The second, meanwhile, is due to the difficulties encountered in fitting experimental spectra in which both CSA and quadrupolar effects contribute significantly to the spinning sideband intensities [40]. It is suggested that the chemical shift, and to a lesser degree, the quadrupolar asymmetry parameters (since C_Q is generally greater than δ_{aniso}) obtained from such fits are likely to display relatively larger inaccuracies.

(iii) Geometry optimisations have been performed for all of the present compounds, given the intended application of the derived shielding reference data to the distorted environ-ments anticipated in doped electrolyte phases. However, the NMR parameters obtained for a subset of the materials using fixed experimental structures reveal no clear system-atic improvement in quality of agreement with experimen-tal data. Again, this may be due to the difficulties involved in reconciling the dynamically- and spatially-averaged structure obtained from diffraction with the local environ-ments experienced by the observed nuclei on the NMR timescale.

(iv) A full optimisation of the LaGaGe$_2$O$_7$ structure provides lat-tice constants and a local GaO$_5$ environment in excellent agreement with the extant experimental data for the iso-structural NdGaGe$_2$O$_7$ compound [68]. Subsequent NMR cal-culations for this unusual coordination yield an isotropic shift lying in the vicinity of the upper experimental range, and C_Q- and η_Q-values in reasonable agreement with the experimental data. The computed CSA, meanwhile, overesti-mates the approximate experimental value by a factor of two, but it is noted that Massiot et al. classed the latter as an initial estimate [59].

On the basis of these results, combined experimental NMR and theoretical studies are currently underway on a range of materials of potential relevance to future ITSOFC technologies, including Mg- and Sr-doped LaGaO$_3$ and associated aluminates (Blanc et al., unpublished data), Ga-doped Ba$_2$In$_2$O$_5$ (Holmes et al., unpublished data), and various analogues of Y-doped BaZrO$_3$ (Buannic et al., unpublished data). Further refinements of the current approach also constitute an interesting line of research. The use of molecular or lattice dynamics calculations could conceivably permit for the incorporation of thermal motion into the computed NMR parame-ters, though this remains a challenging task for the number of

Table 4
Comparison of the experimental and computed properties related to the anisotropy of, asymmetry in and relative orientation of the chemical shift and electric field gradient tensors at ^{71}Ga sites [48,59–69].

Material	Space group	Chemical shift tensor				Quadrupole interaction tensor				$S_{\sigma V}$
		δ_{aniso} (ppm)[expt.]	η_{CS} [expt.]	σ_{aniso} (ppm)[GIPAW]	η_{CS} [GIPAW]	C_Q (MHz) [expt.]	η_Q [expt.]	C_Q (MHz)[GIPAW]	η_Q [GIPAW]	
α-Ga$_2$O$_3$ (oct.)	R$\bar{3}$c [60]			−67.46	0.00	8.2(1) [61] 8.16(1) [62]	0.08(4) [61] 0.00(5) [62]	6.16	0.00	1.000
α-Ga$_2$O$_3$ (expt.) (oct.)	R$\bar{3}$c [60]			−69.13	0.00	8.2(1) [61] 8.16(1) [62]	0.08(4) [61] 0.00(5) [62]	6.55	0.00	1.000
β-Ga$_2$O$_3$ (oct.)	C2/m [63]	−55.5 [69]	0.73(18) [69]	56.84	0.66	8.2(1) [61] 8.34 [62]	0.12(8) [61] 0.1 [62]	4.18	0.87	0.001
(tet.)		49.5 [69]	0.1(2) [69]	−50.78	0.36	11.0(5) [61] 11.1 [62]	0.9(1) [61] 0.85 [62]	−9.11	0.51	0.262
β-Ga$_2$O$_3$ (expt.) (oct.)	C2/m [63]	−55.5 [69]	0.73(18) [69]	55.52	0.85	8.2(1) [61] 8.34 [62]	0.12(8) [61] 0.1 [62]	−5.17	0.99	0.000
(expt.) (tet.)		49.5 [69]	0.1(2) [69]	−49.48	0.37	11.0(5) [61] 11.1 [62]	0.9(1) [61] 0.85 [62]	−9.65	0.54	0.278
LiGaO$_2$ (tet.)	Pna2$_1$ [64]			35.75	0.90	3.89(5) [61]	0.37(2) [61]	−2.71	0.55	0.988
LiGaO$_2$ (expt.) (tet.)	Pna2$_1$ [64]			49.16	0.92	3.89(5) [61]	0.37(2) [61]	−3.98	0.67	0.997
NaGaO$_2$ (tet.)	Pna2$_1$ [65]			−26.28	0.92	3.69(5) [61]	0.40(2) [61]	−2.04	0.80	0.004
GaPO$_4$ (tet.)	P3$_1$21 [66]			−28.07	0.40	8.5(1) [59]	0.45(2) [59]	8.21	0.34	1.000
LaGaO$_3$ (oct.)	Pbnm [48]			30.05	0.46	1.26(9) [61] 1.31(11)[a]	0.5(3) [61] 0.11(6)[a]	−1.49	0.55	0.812
LaGaO$_3$ (oct.)	R3c [67]			7.13	0.00	1.66(6)[a]	0.06(5)[a]	1.66	0.00	1.000
LaGaGe$_2$O$_7$ (5-coord)	P2$_1$/c [68]	∼100 [59]		-183.18	0.75	15.0(3) [59]	0.70(2) [59]	−11.59	0.56	0.060

[a] Blanc et al. (unpublished data).

materials studied here. Moreover, there remain important questions as to the improvements obtainable from treatments of electron exchange and correlation beyond the pure DFT functional applied here, though it is noted that the deployment of such methods within the GIPAW approach is not yet routine.

Appendix A. Supplementary data

Supplementary data associated with this article can be found, in the online version, at doi:10.1016/j.jmr.2010.01.004.

References

[1] B.C. Steele, A. Heinzel, Nature 414 (2001) 345.
[2] J.B. Goodenough, Annu. Rev. Mater. Res. 33 (2003) 9.
[3] T. Ishihara, M. Matsuda, Y. Takita, J. Am. Chem. Soc. 116 (1994) 3801.
[4] T.-Y. Chen, K.-Z. Fung, J. Power Sources 132 (2004) 1.
[5] M. Kajitani, M. Matsuda, A. Hoshikawa, S. Harjo, T. Kamiyama, T. Ishigaki, F. Izumi, M. Miyake, Chem. Mater. 17 (2005) 4235.
[6] M.S. Khan, M.S. Islam, D.R. Bates, J. Phys. Chem. B 102 (1998) 3099.
[7] M. Kilo, M.A. Taylor, C. Argirusis, G. Borchardt, R.A. Jackson, O. Schulz, M. Martin, M. Weller, Solid State Ionics 175 (2004) 823.
[8] M. Feng, J.B. Goodenough, Mater. Res. Symp. Proc. 369 (1995) 333.
[9] G.B. Zhang, D.M. Smyth, Solid State Ionics 82 (1995) 161.
[10] J.B. Goodenough, J.E. Ruiz-Diaz, Y.S. Zhen, Solid State Ionics 44 (1990) 21.
[11] T. Yao, Y. Uchimoto, M. Kinuhata, T. Inagaki, H. Yoshida, Solid State Ionics 132 (2000) 189.
[12] S.B. Adler, J.W. Smith, J.A. Reimer, J. Chem. Phys. 98 (1993) 7613.
[13] S.B. Adler, J.W. Smith, Faraday Trans. Roy. Soc. 89 (1993) 3123.
[14] K. Fuda, K. Kishia, S. Yamauchi, K. Fueki, Phys. Chem. Solids 10 (1985) 1141.
[15] N. Kim, C.P. Grey, Science 297 (2002) 1317.
[16] S.B. Adler, J.A. Reimer, J. Baltisberger, U. Werner, J. Am. Chem. Soc. 116 (1994) 675.
[17] L.A. Holmes, L. Peng, I. Heinmaa, R.-N. Vannier, C.P. Grey, Chem. Mater. 20 (2008) 3638.
[18] L. Frydman, J.S. Harwood, J. Am. Chem. Soc. 117 (1995) 5367.
[19] A. Medek, J.S. Harwood, L. Frydman, J. Am. Chem. Soc. 117 (1995) 12779.
[20] L. Frydman, in: D.M. Grant, R.K. Harris (Eds.), Encyclopaedia of Nuclear Magnetic Resonance, Advances in NMR, vol. 9, John Wiley, Chichester, UK, 2002, p. 262.
[21] M.T. Dove, M. Gambhir, K.D. Hammonds, V. Heine, A.K.A. Pryde, Phase Transitions 58 (1996) 121.
[22] S. Rossano, F. Mauri, C.J. Pickard, I. Farnan, J. Phys. Chem. B 109 (2005) 7245.

[23] J.-N. Dumez, C.J. Pickard, J. Chem. Phys. 130 (2009) 104701.
[24] S.J. Clark, M.D. Segall, C.J. Pickard, P.J. Hasnip, M.J. Probert, K. Refson, M.C. Payne, Z. Kristall. 220 (2005) 567.
[25] C.J. Pickard, F. Mauri, Phys. Rev. B63 (2001) 245101.
[26] J.R. Yates, C.J. Pickard, F. Mauri, Phys. Rev. B76 (2007) 024401.
[27] M. Profeta, F. Mauri, C.J. Pickard, J. Am. Chem. Soc. 125 (2003) 541.
[28] T. Charpentier, S. Ispas, M. Profeta, F. Mauri, C.J. Pickard, J. Phys. Chem. B 108 (2004) 4147.
[29] R.K. Harris, S.A. Joyce, C.J. Pickard, S. Cadars, L. Emsley, Phys. Chem. Chem. Phys. 8 (2006) 137.
[30] F. Blanc, J.-M. Basset, C. Copéret, A. Sinha, Z.J. Tonzetich, R. Schrock, X. Solans-Montfort, E. Clot, O. Eisenstein, L. Lesage, L. Emsley, J. Am. Chem. Soc. 130 (2008) 5886.
[31] S.E. Ashbrook, M. Cutajar, C.J. Pickard, R.I. Walton, S. Wimperis, Phys. Chem. Chem. Phys. 10 (2008) 5754.
[32] J.P. Perdew, K. Burke, M. Ernzerhof, Phys. Rev. Lett. 77 (1996) 3865.
[33] P. Pyykkö, Mol. Phys. 99 (2001) 1617.
[34] G. Vidal-Valat, J.P. Vidal, K. Kurki-Suonio, R. Kurki-Suonio, Acta Cryst. A43 (1987) 540.
[35] G.L. Turner, S.E. Chung, E. Oldfield, J. Magn. Reson. 64 (1985) 316.
[36] J.-Z. Zhao, L.-Y. Lu, X.-R. Chen, Y.-L. Bai, Physica B Condens. Matter 387 (2007) 245.
[37] D. Taylor, Trans. Br. Ceram. Soc. 83 (1984) 5.
[38] L.-G. Liu, W.A. Bassett, J. Geophys. Res. 77 (1972) 4934.
[39] T. Yamanaka, N. Hirai, Y. Komatsu, Am. Miner. 87 (2002) 1183.
[40] T.J. Bastow, P.J. Dirken, M.E. Smith, H.J. Whitfield, J. Phys. Chem. 100 (1996) 18539.
[41] I. Levin, T.G. Amos, S.M. Bell, L. Farber, T.A. Vanderah, R.S. Roth, B.H. Toby, J. Solid State Chem. 175 (2003) 170.
[42] Y. Hinatsu, J. Solid State Chem. 122 (1996) 384.
[43] S.A. Hayward, S.A.T. Redfern, H.J. Stone, M.G. Tucker, K.R. Whittle, W.G. Marshall, Z. Kristall. 220 (2005) 735.
[44] V. Anuradha, Masters thesis, University of Warwick, UK, 1990.
[45] G.H. Kwei, A.C. Lawson Jr., S.J.L. Billinge, S.-W. Cheong, J. Phys. Chem. 97 (1993) 2368.
[46] D.R. Spearing, J.F. Stebbins, J. Am. Ceram. Soc. 77 (1994) 3263.

[47] S.A. Hayward, F.D. Morrison, S.A.T. Redfern, E.K.H. Salje, J.F. Scott, K.S. Knight, S. Tarantino, A.M. Glazer, V. Shuvaeva, P. Daniel, M. Zhang, M.A. Carpenter, Phys. Rev. B72 (2005) 054110.
[48] R.J. Angel, J. Zhao, N.L. Ross, C.V. Jakeways, S.A.T. Redfern, M. Berkowski, J. Solid State Chem. 180 (2007) 3408.
[49] B.J. Kennedy, C.J. Howard, B.C. Chakoumakos, Phys. Rev. B59 (1999) 4023.
[50] D.P. Dobson, S.D. Jacobsen, Am. Miner. 89 (2004) 807.
[51] S.E. Ashbrook, A.J. Berry, D.J. Frost, A. Gregorovic, C.J. Pickard, J.E. Readman, S. Wimperis, J. Am. Chem. Soc. 129 (2007) 13213.
[52] W. Fischer, G. Reck, T. Schober, Solid State Ionics 116 (1999) 211.
[53] S.A. Speakman, J.W. Richardson, B.J. Mitchell, S.T. Misture, Solid State Ionics 149 (2002) 247.
[54] M. Profeta, M. Benoit, F. Mauri, C.J. Pickard, J. Am. Chem. Soc. 126 (2004) 12628.
[55] F. Corà, M. Alfredsson, G. Mallia, D.S. Middlemiss, W.C. Mackrodt, R. Dovesi, R. Orlando, Struct. Bonding 113 (2004) 171.
[56] Q. Zhang, T. Cagin, W.A. Goddard III, Proc. Natl. Acad. Sci. 103 (2006) 14695.
[57] M.B. Smith, K. Page, T. Siegrist, P.L. Redmond, E.C. Walter, R. Seshadri, L.E. Brus, M.L. Steigerwald, J. Am. Chem. Soc. 130 (2008) 6955.
[58] M.I. Marqués, C. Aragó, J.A. Gonzalo, Phys. Rev. B 72 (2005) 092103.
[59] D. Massiot, T. Vosegaard, N. Magneron, D. Trumeau, V. Montouillout, P. Berthet, T. Loiseau, B. Bujoli, Solid State Nucl. Magn. Reson. 15 (1999) 159.
[60] M. Marezio, J.P. Remeika, J. Chem. Phys. 46 (1967) 1862.
[61] J.T. Ash, P.J. Grandinetti, Magn. Reson. Chem. 44 (2006) 823.
[62] L.A. O'Dell, S.L.P. Savin, A.V. Chadwick, M.E. Smith, Appl. Magn. Reson. 32 (2007) 527.
[63] J. Ahman, G. Svensson, J. Albertsson, Acta Cryst. C 52 (1996) 1336.
[64] G.M. Kuz'micheva, V.B. Rybakov, A.V. Gaister, E.V. Zharikov, Inorg. Mater. 37 (2001) 281.
[65] H. Mueller, R. Hoppe, Z. Anorg. Allegmeine Chem. 611 (1992) 73.
[66] H. Nakae, K. Kihara, M. Okuno, S. Hirano, Z. Kristall. 210 (1995) 746.
[67] P.R. Slater, J.T.S. Irvine, T. Ishihara, Y. Takita, J. Solid State Chem. 139 (1998) 135.
[68] O. Jarchow, K.H. Klaska, Z. Kristall. 172 (1985) 159.
[69] T. Vosegaard, I.P. Byriel, L. Binet, D. Massiot, H.J. Jakobsen, J. Am. Chem. Soc. 120 (1998) 8184.
[70] R.D. Shannon, Acta Cryst. A 32 (1976) 751.